

In vivo characterization of electroactive biofilms inside porous electrodes with MR Imaging

Electronic Supplementary Information (ESI)

Luca Häuser^a, Johannes Erben^b, Guillaume Pillot^a, Sven Kerzenmacher^{*a}, Wolfgang Dreher^c
and Ekkehard Küstermann^c

^a Center for Environmental Research and Sustainable Technology (UFT), University of Bremen, 28359 Bremen, Germany

^b Electrochaea GmbH, 82152 Planegg, Germany

^c In-vivo-MR Group, Faculty 02 (Biology/ Chemistry), University of Bremen, 28359 Bremen, Germany

MR image acquisition and processing

Figure S1 shows a schematic diagram of the MR image acquisition (parameters see in Tab. S1) and subsequent processing. Transmission of radiofrequency (RF) pulses with spin-echo sequences and reception of the corresponding MR signals was done by the RF-coil. By Fourier transformation, these signals echoes were transferred into the image space where an area covering the electrode and adjacent medium were selected as the specific region of interest (ROI). Therein voxels with no signals were declared as defective and masked. Afterwards the ROI was filtered with a Gaussian filter. T_2 (D_*) maps were calculated from the exponential fit of the echo signals. The deep z-profiles of $T_{2,rel}^{slice}$ ($D_{*,rel}^{slice}$) were calculated as mean value from all voxels in each slice parallel to the electrode surface (z-direction).

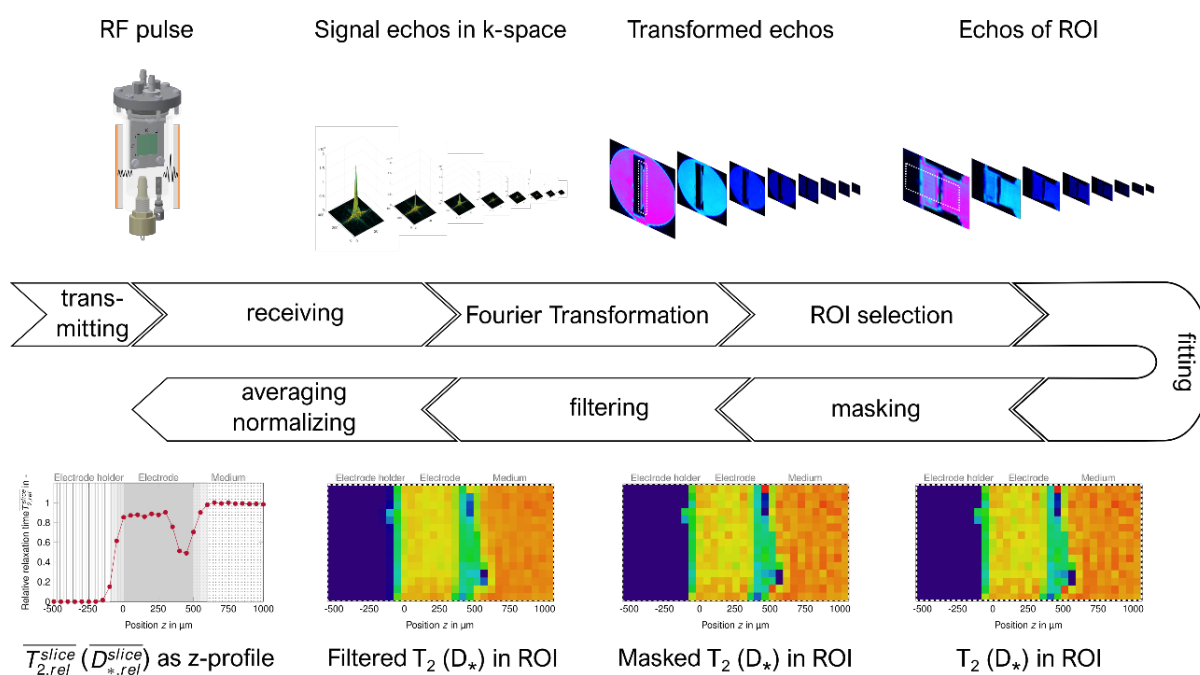


Figure S1: Image acquisition and processing here exemplarily visualized as T_2 -weighted imaging of the biofilm inside the improved medium M^* .

Table S1: MRI acquisition parameters for abiotic and biotic experiments in the standard medium M and in the improved medium M*. Spin-echo MR sequences were used for T_2 -weighted (Multi-Slice Multi-Echo – ‘MSME’) and Spin-Echo Diffusion Weighted imaging (‘SEDW’) to determine the transversal relaxation time T_2 and the apparent diffusion coefficients (D_*).

	Standard medium M		Standard medium M		Improved medium M*	
Biofilm	no		yes		yes	
Sequence	MSME	SEDW	MSME	SEDW	MSME	SEDW
Echotime TE in ms	20	29	20	29	20	28
Number of echos in -	8	4	8	4	8	4
b -values in s mm ⁻²		50;350;650;950		50;350;650;950		50;350;650;950
Repetitiontime TR in ms	500	500	500	500	500	500
Acquisition matrix (z y x)	384×96×100	384×32×33	384×96×100	384×96×100	384×32×33	384×32×33

Fluorescence microscopy and biofilm density quantification with MRI, current correlation, and qPCR

After image acquisition the reactor was deconstructed and the biofilm in the electrode was fixated using a 2.5 % glutaraldehyde solution. The fixated biofilm was treated with the fluorescent stain acridine orange. A Zeiss microscope Axioscope 5/7 (Solid-State Light source Colibri 3 (Type RGB-UV), Microscopy Camera AxioCam 702 mono) (Zeiss, Deutschland) with 250× magnification (objective ApoChrom 25×) was used to visualize marked cells. Total amount of cells was counted from z-projected images with the software CellC12.

Subsequently the biofilm was dissolved and the total number of *S. oneidensis* cells n_{So} and bacteria cells n_b were determined by the qPCR. The 16S rRNA gene of the cell suspensions previously obtained was partially amplified by the qPCR method in an Eco 48 Real Time PCR System (PCRmax, United Kingdom), using the qPCRBio SyGreen 2x-Mix (Nippon Genetics Europe, Germany), and the primers She211F (5'-CGCGATTGGATGAACCTAG-3')¹ and Univ516R (5'-GTDTTACCGCGGCKGCTGRCA-3')². The PCR program was composed of a 5 min initial denaturation step at 98°C followed by 50 cycles of 10s denaturation step at 98°C, a hybridization step of 20 s at 55°C and a 40 s elongation step at 72°C, with melting curves generated at the end of each reaction to ensure product specificity. A standard curve was prepared through cloning method using pGEM(R)-T Easy Vector System II (Promega) and JM109 Competent Cells (Promega). The plasmid was extracted with PureYield™ Plasmid Miniprep System (Promega) and quantified on a Quantus™ Fluorometer using the QuantiFluor(R) dsDNA System (Promega). The quantification of copies of 16S rDNA was divided by the number of copies naturally present per cell (9 copies·per cell according to rrnDB database), to obtain the number of *S. oneidensis* cells n_{So} and bacteria cells n_b .

To estimate the biofilm density \overline{X}^{elec} in the entire electrode volume V^{elec} , the averaged diffusion coefficient in the entire electrode $\overline{D}_{*,rel}^{elec}$ was used in the empirical correlation.¹⁰ \overline{X}_D^{elec} is compared to the mean biofilm density determined by biomass specific current production \overline{X}_i^{elec} and the cell density determined by total MR-1 cell count via qPCR \overline{X}_{So}^{elec} :

The mean biofilm density \overline{X}_i^{elec} was calculated with the biomass specific current production $i_m = 65.2 \mu A mg^{-1}$ according to $\overline{X}_i^{elec} = I / (i_m \cdot V^{elec})$.⁸

The biofilm density is thus given by $\overline{X}_{So}^{elec} = n_{So} \cdot m_{cell} / V^{elec}$ using an estimated cell weight of $m_{cell} = 10^{-12}$ g. The cell count of the *S. oneidensis* primer has been validated by qPCR with universal bacteria primers.

Interpretation of MR Images and their impact on resolving the biofilm

Transversal relaxation time T_2 maps and the corresponding courses of the $\overline{T_{2,rel}^{slice}}$ -profiles averaged over the entire slice are shown for the standard medium M in Figure S2a and for the improved medium M* in Figure S2b. In addition to the electrode, biofilm and medium regions already shown, the electrode holder region is also shown. In the electrode holder region ($z < -200 \mu\text{m}$) the T_2 -times (and D_*) are close to zero, due to short ^1H relaxation times in the plastic of the electrode holder. This region is not considered in publications of Renslow³⁻⁵. It is noteworthy that no influence of metallic materials (either for contacting the electrode or the electrode itself) on MR imaging are visible.

The values of $\overline{T_{2,rel}^{slice}}$ (and $\overline{D_{*,rel}^{slice}}$) in the transition region ($-200 \mu\text{m} \leq z \leq 0 \mu\text{m}$) range between the values of plastic (0) and the growth medium (1). Surface roughness of the electrode holder, partial volumes including voxels from holder and electrode/medium and the misalignment of the electrode backside (only in the standard medium M) due non-parallel mounting cause an increase of the $\overline{T_{2,rel}^{slice}}$ (and $\overline{D_{*,rel}^{slice}}$) in several slices (transition region between holder and electrode):

First, surface roughness of the electrode holder (filled with medium, Fig. S2c) increases $\overline{T_{2,rel}^{slice}}$ (and $\overline{D_{*,rel}^{slice}}$).

Second, voxels including partial volumes from both the electrode holder and the (porous electrode filled with) growth medium are in between zero and T_2^{aq} (D_*^{aq}). In Fig. S2, voxels with partial volumes or low biofilm density can be identified by their cyan to green color (at $z \sim 0 \mu\text{m}$, Fig. S2d).

Third, only in the standard medium M the electrode probably has not been mounted planar which results in a misalignment of MR voxel relative to the backside of electrode (Fig. S2e). The non-planar mounting results in different thicknesses of the porous electrode indicated by the arrows in Fig. S2f). However, Fig. S2 also shows that the ROI is aligned correctly to front side of the electrode.

The voxels at the interface of electrode to medium are also affected by subvolumes of both electrode and pure medium and by grown up inhomogeneous biofilm and thus result in an unsharp boundary illustrated in shades of grey in Fig. S3b.

The above-described phenomena (in T_2 -maps in Fig. S2 and D_* -maps in Fig. S4) render the accurate quantification of the biofilm at the backside of the electrode with current reactor design impossible. However, from fluorescence microscopy we know, that at the backside of the electrode cells were attached (see below). But the reduced MRI signal in this region cannot be further differentiated i.e., attributed to the plastic of the electrode holder/transition region or to the biofilm as the cause. A qualitative comparison of abiotic to biotic $\overline{T_{2,rel}^{slice}}$ courses might indicate that the back side has taken up only little amount of biofilm compared to the front side.

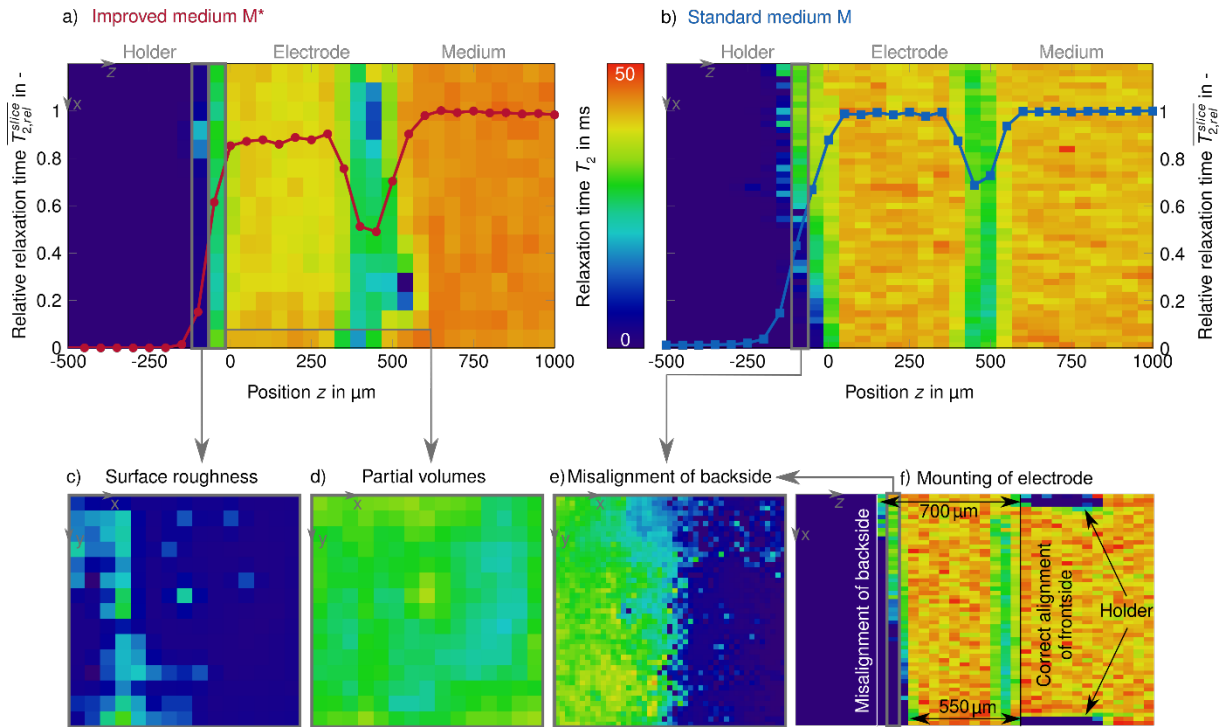
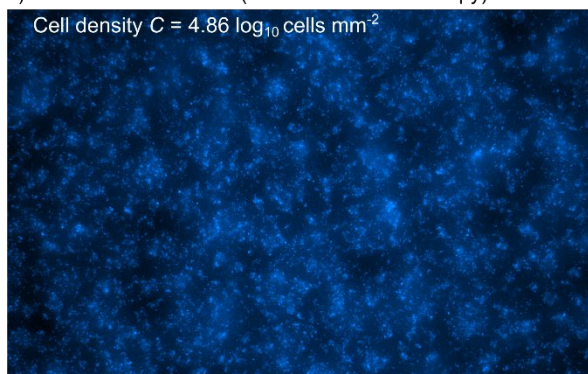


Figure S2: Results of transversal relaxation time T_2 -weighted imaging of the electrode with biofilm and the electrode holder illustrated as representative T_2 heat maps and corresponding depth profiles for the improved medium M^* (a) and the standard medium M (b). The increase of the $\overline{T_{2,rel}^{slice}}$ times in several slices in the transition region between holder and electrode ($-200 \mu\text{m} \leq z \leq 0 \mu\text{m}$) is a result of surface roughness of the electrode holder (c), partial volumes including voxels from holder and electrode/medium (d) and the misalignment of the electrode backside (e). The misalignment was only observed in the standard medium M and is related to a non-planar mounting of the electrode (f) indicated by different distances between the electrode holders (arrows, $700 \mu\text{m}$ vs $550 \mu\text{m}$).

Biofilm distribution within and at the boundaries of the electrode

Fluorescence microscopy (Fig. S3a and S3c) indicate that biofilm is located not only at the fluid facing frontside but also on the backside of the electrode. However, the biofilm distribution within the entire electrode (thickness $d \sim 500 \mu\text{m}$) is not accessible by fluorescence microscopy due to the limited penetration of about $10 \mu\text{m}$. MRI shows that the central region of the porous electrode filled with growth medium is almost uncolonized as T_2 and D_* values are close to the values in the medium (no difference to abiotic electrode).

a) Backside of electrode (fluorescence microscopy)



b) Frontside of electrode (fluorescence microscopy)

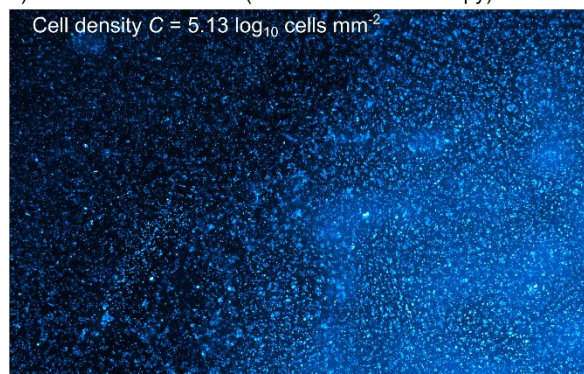


Figure S3: Biofilm formation in the improved medium M: Fluorescence microscopy revealed that biofilm was also located at the electrode backside facing the holder (a) and confirmed that the electrode was colonized highly at the frontside facing the medium (b).*

Determination of biofilm density inside the electrode

Figure S4a and S4b shows D_* maps and the corresponding courses of the averaged $\overline{D_{*,rel}^{slice}}$ profiles for biofilms in both media. As already discussed, there is a high similarity between $\overline{D_{*,rel}^{slice}}$ and $\overline{T_{2,rel}^{slice}}$, and there are the same origins of the $\overline{D_{*,rel}^{slice}}$ increase in several slices from holder to electrode (described above for $\overline{T_{2,rel}^{slice}}$).

Diffusion coefficients in the bulk medium follow a statistical distribution (Fig. S4e). It can be assumed that this true for the other region (exceptions see below). In general, higher resolution of diffusion coefficients translates to higher signal to noise ratio. More noise is expressed as broader distribution of D_* (and T_2) and thus in a higher standard deviation. According to these phenomena, the highest standard deviations of relative MRI parameters - $\overline{T_{2,rel}^{slice}}$ and $\overline{D_{*,rel}^{slice}}$ in bulk water - is found in D_* in the standard medium M (see Tab. S1). Neither in the standard medium M nor in the improved medium M*, noise influences averaged $\overline{D_{*,rel}^{slice}}$, but there is a significant effect on the calculated biofilm density distribution.

In principle, there are two ways to calculate the biofilm density from the spatial diffusion coefficients and using Fan's correlation: First, using already averaged diffusion coefficients $\overline{D_{*,rel}^{slice}}$ or $\overline{D_{*,rel}^{elec}}$ (mean-to-mean approach, see main publication) and second determining biofilm density in individual voxel from corresponding diffusion coefficients D_* and subsequently averaging in slices or averaging for the entire electrode (voxel-to-mean approach). Both approaches are associated with problems due to the non-linearity of the Fan equation (Fig. S4f):

First, the noise expressed by the standard deviation of the statistical distribution of diffusion coefficients is neglected using mean-to-mean approach but overestimated using voxel-to-mean approach.

Second, the biofilm in the electrode ($0 \mu\text{m} \leq z \leq 600 \mu\text{m}$) alters the distribution of D_* and thus mean-to-mean approach underestimates biofilm density. On the other hand, voxel-to-mean approach considers a D_* distribution distorted by the biofilm e.g., as a result of partial volumes/weak biofilm at the interface (Fig. S4c) or from inhomogeneities (round shape of the biofilm in the improved medium M* might be related to tension caused by the holder, Fig. S4d).

The true biofilm density might be in the range between the values determined with mean-to-mean approach and voxel-to-mean approach. In both calculation methods, the determined biofilm densities were subsequently normalized. The normalization contribution corresponds to the biofilm density of the uncolonized electrode and should eliminate noise. For this reason, it can be assumed that the true biofilm density is sufficiently approximated by the voxel-to-mean method. Nevertheless, the mean-to-mean method, as used in the publication, is capable to specify confidence intervals and thereby sensitized to the uncertainties of the determination of biofilm density with the empirical Fan correlation.

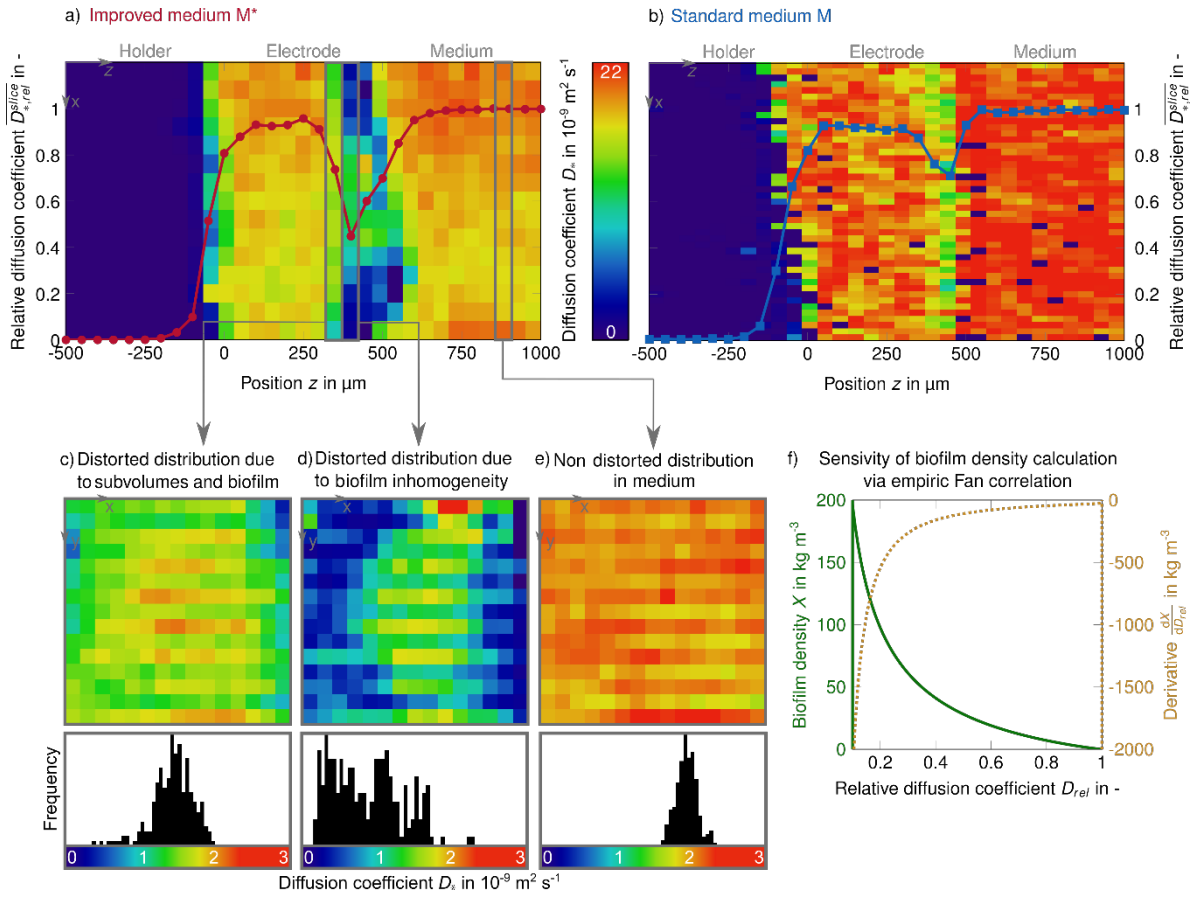


Figure S4: Diffusion-weighted imaging of the electrode with biofilm and the electrode holder as representative diffusion coefficient D_* heat maps, corresponding depth profiles $\overline{D_{*,rel}^{slice}}$ for the improved medium M* (a) and the standard medium M (b). The biofilm density differs depending on the method used due to the non-linear fan correlation (f). If the biofilm density is calculated from mean diffusion coefficients, noise (e) but also biofilm (distortion due to its density and to subvolumes (c) and inhomogeneities (d)) are not taken into account. With the determination of the local biofilm density and subsequent averaging, both effects (noise and biofilm) are considered.

Validation of biofilm density

We validated the biofilm density calculated from MRI diffusion coefficient measurements directly against values obtained by qPCR and indirectly against values estimated by biomass specific current production. Figure S5 shows a comparison of the resulting mean biofilm densities to the mean relative diffusion coefficient ($\overline{D_{*,rel}^{elec}}$ in improved medium M* is 0.769 ± 0.046 , $\overline{D_{*,rel}^{elec}}$ in standard medium M is 0.870 ± 0.087). The values obtained by MRI and alternate methods show the same trend for the different growth media M and M*. Diffusion coefficients $\overline{D_{*,rel}^{elec}}$, the cell count n_{So} (specified via qPCR of 16S rDNA copies with primers specific to *S. oneidensis* MR-1) and biomass specific current i_m production paint a coherent picture of the biofilm density. However, the values obtained differ in about one order of magnitude. These discrepancies might be explained by the following:

- As qPCR does not account the EPS-matrix, the biofilm density might be underestimated.⁶ Indeed, EPS are known to be excessively produced during biofilm formation.⁷ Even if EPS contributes to extracellular electron transfer by conducting electrons, it does not produce current.
- Sample storage and treatment prior to qPCR through sonication has not been optimized for the porous electrode. Furthermore, the biofilm might not have been completely lysed during this treatment. The resulting underestimation of the total cell density makes precise comparison difficult. However, this can be enabled in the future by optimizing the method.
- The biofilm density determination by biomass specific current production i_m underestimates the biofilm density due to the fact, that the biomass specific current was determined at a temperature of 30°C (21°C – 22°C in our experiments). This underestimation leads to even higher discrepancies in biofilm densities.

The discrepancy underlines the relevance of a second, validating method, although all methods/all biofilm densities show the same trend. We therefore assume that the biofilm density values and profiles presented here are to be interpreted in a semiquantitative or qualitative manner.

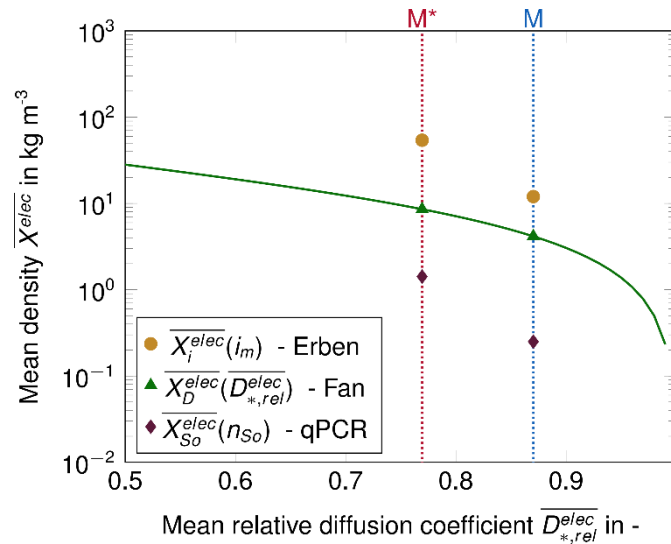


Figure S5: Mean densities derived from biomass normalized currents i_m from (Erben et al. 2021c), by relative diffusion coefficients $\overline{D_{*,rel}^{elec}}$ according to Fan (Fan et al. 1990) and by the total count of *S. oneidensis* cells n_{So} quantified with qPCR displayed versus mean relative diffusion coefficient $\overline{D_{*,rel}^{elec}}$ determined with diffusion-weighted MRI.

Biofilm attachment after current breakdown in the standard medium M

During the experiment with the standard medium M, the current production of the EAB dropped to approximately zero due to an error of the reference electrode. However, a control T_2 -measurement after the electrical error revealed that the biofilm was still attached to the electrode as Figure S7 (in comparison to Fig. S2b) shows.

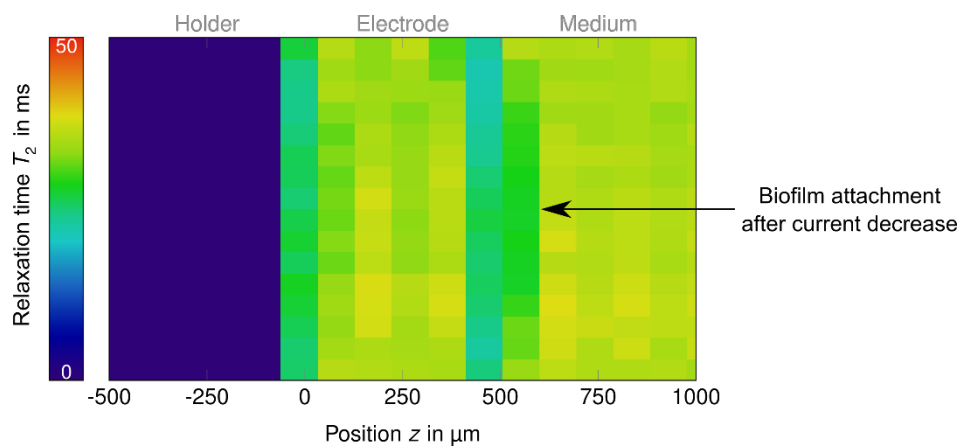


Figure S7: Biofilm attachment after current decreases due to an electrical error of the reference electrode in the standard medium M revealed by a T_2 control measurement after the electrical error.

Optical density and pH in the medium

In both media ($z \leq 600 \mu\text{m}$), the optical density was always below 0.1, indicating no planktonic cell growths (Fig. S8). The pH inside the bulk medium is stable throughout the entire experimental time (Fig. S8).

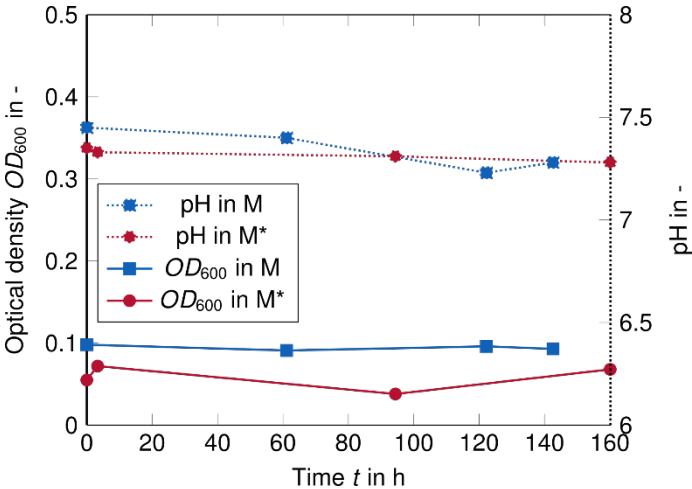


Figure S8: Optical density and pH in bulk medium over time for standard medium M and improved medium M*.

Table S2: Experimental, electrochemical, Magnetic Resonance Imaging and biofilm density values for the standard medium M and the improved medium M*.

	Unit	Standard medium M	Improved medium M*
Experiment			
Medium PBS concentration	mmol/l	10	40 + 0.001 Riboflavin
Microorganism	-	<i>S. oneidensis</i> MR-1	<i>S. oneidensis</i> MR-1
Anode material according to Erben et al. ⁸	-	6 wt PAN EC	6 wt PAN EC
Electrochemistry			
Potential E (vs Aq/AqCl)	mV	0	0
Maximum current I_{max}	μ A	68.93	280.16
Maximum current density i_{max}	μ A cm ⁻²	68.93	280.16
Magnetic Resonance Imaging			
Transversal relaxation			
Relaxation time in abiotic medium/water T_2^{aq}	ms	39.4 ± 2.3	56.5 ± 0.9
Relaxation time in biotic medium/water T_2^{aq}	ms	40.9 ± 1.4	44.5 ± 0.8
Minimum of relative slice relaxation time $\overline{T_{2,rel}^{slice}}$	-	0.686 ± 0.035	0.490 ± 0.018
Apparent diffusion coefficients			
Diffusion coefficient in abiotic medium/water D_+^{aq}	m ² s ⁻¹	1.97 ± 0.22	1.87 ± 0.07
Diffusion coefficient in biotic medium/water D_+^{aq}	m ² s ⁻¹	2.00 ± 0.16	1.94 ± 0.09
Temperature T according to Simpson and Carr ⁹	°C	22.4 (19.2, 25.4)	21.3 (19.6, 23.0)
Minimum of relative slice diffusion coefficient $\overline{D_{+rel}^{slice}}$	-	0.713 ± 0.087	0.448 ± 0.046
Biofilm densities			
Diffusion coefficient			
Maximum slice biofilm density $\overline{X^{slice}}$ according to Fan et al. ¹⁰	kg m ⁻³	9.6 (7.1, 17.1)	32.8 (28.8, 40.7)
Mean biofilm density from electrode diffusion coefficient $\overline{X_h^{elec}}$	kg m ⁻³	4.2 (1.2, 7.9)	8.6 (6.4, 11)
qPCR			
Bacteria			
Cell count n_b per electrode	log ₁₀ cells	7.21	7.79
Mean biofilm density from bacteria count $\overline{X_h^{elec}}$	kg m ⁻³	0.33	1.25
Shewanella			
Cell count n_{So} per electrode	log ₁₀ cells	7.09	7.85
Mean biofilm density from S.o. count $\overline{X_{So}^{elec}}$	kg m ⁻³	0.25	1.42
Biomass normalized currents			
Current per biomass i_m according Erben et al. ⁸	μ A mg ⁻¹	65.2 ± 7	65.2 ± 7
Mean biofilm density from current $\overline{X_l^{elec}}$	kg m ⁻³	21.2	86.2

References

Journal articles

- 1 S. G. Todorova and A. M. Costello, Design of Shewanella-specific 16S rRNA primers and application to analysis of Shewanella in a minerotrophic wetland, *Environmental microbiology*, 2006, **8**, 426–432.
- 2 K. Takai and K. Horikoshi, Rapid detection and quantification of members of the archaeal community by quantitative PCR using fluorogenic probes, *Applied and environmental microbiology*, 2000, **66**, 5066–5072.
- 3 R. S. Renslow, P. D. Majors, J. S. McLean, J. K. Fredrickson, B. Ahmed and H. Beyenal, In situ effective diffusion coefficient profiles in live biofilms using pulsed-field gradient nuclear magnetic resonance, *Biotechnology and bioengineering*, 2010, **106**, 928–937.
- 4 R. Renslow, J. Babauta, A. Dohnalkova, M. Boyanov, K. Kemner, P. Majors, J. Fredrickson and H. Beyenal, Metabolic spatial variability in electrode-respiring *Geobacter sulfurreducens* biofilms, *Energy & environmental science*, 2013, **6**, 1827–1836.
- 5 R. Renslow, J. Babauta, P. Majors and H. Beyenal, Diffusion in biofilms respiring on electrodes, *Energy & environmental science*, 2013, **6**, 595–607.
- 6 A. Gędas and M. A. Olszewska, in *Recent trends in biofilm science and technology*, ed. M. Simões, A. Borges and L. C. Simões, Academic Press, London, United Kingdom, San Diego, CA, 2020, pp. 1–21.
- 7 L. Gao, X. Lu, H. Liu, J. Li, W. Li, R. Song, R. Wang, D. Zhang and J. Zhu, Mediation of Extracellular Polymeric Substances in Microbial Reduction of Hematite by *Shewanella oneidensis* MR-1, *Front. Microbiol.*, 2019, **10**, 575.
- 8 J. Erben, X. Wang and S. Kerzenmacher, High Current Production of *Shewanella Oneidensis* with Electrospun Carbon Nanofiber Anodes is Directly Linked to Biofilm Formation**, *ChemElectroChem*, 2021, **8**, 1836–1846.
- 9 J. H. Simpson and H. Y. Carr, Diffusion and Nuclear Spin Relaxation in Water, *Phys. Rev.*, 1958, **111**, 1201–1202.
- 10 L. S. Fan, R. Leyva-Ramos, K. D. Wisecarver and B. J. Zehner, Diffusion of phenol through a biofilm grown on activated carbon particles in a draft-tube three-phase fluidized-bed bioreactor, *Biotechnology and bioengineering*, 1990, **35**, 279–286.